Accepted Manuscript

Title: sUltra-thin Iron Phosphate Nanosheets for High Efficient U(VI) Adsorption

Authors: De Wang, Yanbin Xu, Difei Xiao, Qingan Qiao, Ping Yin, Zhenglong Yang, Jiaxing Li, William Winchester, Zhe Wang, Tasawar Hayat

PII: S0304-3894(19)30234-1
DOI: https://doi.org/10.1016/j.jhazmat.2019.02.091
Reference: HAZMAT 20360

To appear in: *Journal of Hazardous Materials*

Received date: 4 November 2018
Revised date: 3 February 2019
Accepted date: 25 February 2019

Please cite this article as: Wang D, Xu Y, Xiao D, Qiao Q, Yin P, Yang Z, Li J, Winchester W, Wang Z, Hayat T, sUltra-thin Iron Phosphate Nanosheets for High Efficient U(VI) Adsorption, *Journal of Hazardous Materials* (2019), https://doi.org/10.1016/j.jhazmat.2019.02.091

Ultra-thin Iron Phosphate Nanosheets for High Efficient U(VI) Adsorption

De Wang[a], Yanbin Xu[a,*] , Difei Xiao[a], Qingan Qiao[a], Ping Yin[a], Zhenglong Yang[a], Jiaxing Li[b,*] , William Winchester[c], Zhe Wang[c,*] , Tasawar Hayat[d]

[a]School of Chemistry and Materials Science, Ludong University, Yantai 264025, PR China

[b]CAS Key Laboratory of Photovoltaic and Energy Conservation Materials, Institute of Plasma Physics, Chinese Academy of Sciences, P.O. Box 1126, Hefei 230031, PR China

[c]Chemistry Department, Xavier University of Louisiana, New Orleans, LA, 70125, USA

[d]NAAM Research Group, Faculty of Science, King Abdulaziz University, Jeddah 21589, Saudi Arabia

[*]Corresponding Authors, *Email: xuyanbin@ldu.edu.cn; lijx@ipp.ac.cn; zwang@xula.edu

[*]Corresponding author. Tel.: +86 535 6693762, Fax: +86 535 6693762
E-mail addresses: xuyanbin@ldu.edu.cn; lijx@ipp.ac.cn; zwang@xula.edu

Graphical aabstract

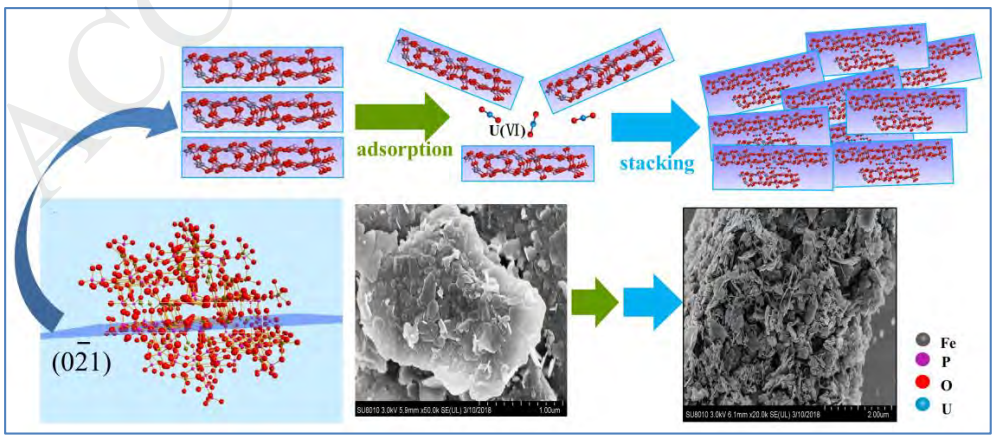

Highlights

- Two-dimensional $Fe_7(PO_4)_6$ was synthesized with an organic solvent refluxing method.
- Adsorption capacity of 2D $Fe_7(PO_4)_6$ for U(VI) achieves to 704.23 $mg \cdot g^{-1}$.
- U(VI) adsorption on 2D $Fe_7(PO_4)_6$ is an endothermic and spontaneous process.

Abstract

In this study, the ultra-thin iron phosphate $Fe_7(PO_4)_6$ nanosheets (FP1) with fine-controlled morphology, has been designed as a new two-dimensional (2D) material for uranium adsorption. Due to its unique high accessible 2D structure, atom-dispersed phosphate/iron anchor groups and high specific surface area (27.77 $m^2 \cdot g^{-1}$), FP1 shows an extreme-high U(VI) adsorption capacity (704.23 $mg \cdot g^{-1}$ at 298 K, pH = 5.0 ± 0.1), which is about 27 times of conventional 3D $Fe_7(PO_4)_6$ (24.51 $mg \cdot g^{-1}$ -sample FP2) and higher than most 2D absorbent materials, showing a great value in the treatment of radioactive wastewater. According to the adsorption results, the sorption between U(VI) and FP1 is spontaneous and endothermic, and can be conformed to single molecular layer adsorption. Based on the analyses of FESEM, EDS, Mapping, FT-IR and XRD after adsorption, the possibile adsorption mechanism can be described as a Monolayer Surface Complexation and Stacking mode (MSCS-Mode). Additionally, the research not only provide a novel preparing method for 2D phosphate materials but also pave a new pathway to study other two-dimensional adsorption materials.

Keywords: 2D materials, $Fe_7(PO_4)_6$, U (VI), adsorption, nanosheets

1. Introduction

Uranium, as one of the vital radionuclides and a key fuel for nuclear reactors, has been widely used in many fields, such as nuclear power plant, medical research, the war industry, and so on [1, 2]. Uranium is a long-lived and high perniciousness radionuclide with a number of radioactive daughter products that inevitably has a harmful effect on human health and ecological in the process of exploitation and application [1-5]. Currently, many reserve approaches, including chemical precipitation [6], electrodeposition [7], ion exchange [8, 9] adsorption [10-17] and ultrafiltration [18], have been investigated to the recycling of radioactive wastes. Due to the continuously increased demand of uranium resources, reserve methods with high efficiency, wide adaptability and environmental friendliness are just beginning to emerge [3-5]. Considering superiority of above factors, adsorption has been considered as a most facile and promising method for the treatment of radionuclides, because of its low-costing, simple operation and high efficiency [19-26].

Uranium(VI), the thermodynamically stable valence of U, is the major U contamination in the soil and ground waters. Choosing a suitable content and morphology of adsorbent, which retains high specific area and strong interaction with U(VI), is considered as the significant key for improving adsorption capacity and stability of the adsorbent [27-32]. Most recently, phosphate based adsorbents [22, 33-39], especially, inorganic phosphate, such as ZrP_2O_7, $Zr_2O(PO_4)_2$, $Th_4(PO_4)_4P_2O_7$ [38, 39], $LaPO_4$ [37] have been reported for U(VI)

adsorption, since the strong chelation or complexation between phosphates and U(VI), along with phosphates' excellent shielding effect on radioactive ions and extremely low solubility [22, 37-40]. However the usage of highly toxic metal ions (Th, Zr and La) and the limited specific surface area are extremely limited their application.

Iron phosphate, as an environmental-friendly phosphate, were mainly applied in areas of work involving catalysts [41], ceramic glass [42], adsorption [43, 44], steel and surface passivation [45], based on its non-pollution, low price and excellent physical and chemical properties [41-46]. In the wide environment, U(VI) could strongly assiciate with solid minerals, in particular, iron-containing phases, as reported for controlling U(VI) adsorption and transportation [47, 48]. As a combination, iron phosphate was expected to be an idea candidate material for U(VI) adsorption. Xu's group [36] reported $Fe_4(P_2O_7)_3$ adsorbent has the excellent stability which granted by the strong interaction with U(VI). However, its adsorption capacity is low (14.92 $mg \cdot g^{-1}$), since the low usage of the functional groups in this 3D structure. The excellent adsorption performance of two-dimensional materials(e.g. grapheme oxide-manganese oxide [49], MXene [50], MoS_2 [51] LDHs [52, 53]) in the field of radioactive adsorption indicates that increasing the specific surface area of materials is an extremely effective means to improve their adsorption performance. Li's group [40] dispersed phosphate groups on the graphene oxide (PGO) nanosheets with a chemical process to increase the usage of phosphate group. It shows a higher adsorption capacity of U(VI) (251.7 $mg \cdot g^{-1}$) than graphene oxide (138.2 $mg \cdot g^{-1}$), revealing that the 2D structure granted dispersion enhance the usage of phosphate group for U(VI) adsorption. But the potential environmental hazard and high preparation cost of graphene oxide greatly limit its application

in the field of adsorption [54-63].

Inspired by above works, we raise a hyposis that a nano-structured 2D iron phosphate may maximize the usage of both Fe and phosphate for U(VI) adsorption, which will ensure the stability of adsorption. And also the fine-controlled morphology without additional supporting materials would provide abundant sorption sites that could enhance adsorption capacity. In this work, a novel iron phosphate ($Fe_7(PO_4)_6$) nuclide adsorption functional materials with two-dimensional structure are designed and fabricated. As shown in Fig. 1, the $(0\bar{2}1)$ crystal plane were peeled off from the $Fe_7(PO_4)_6$ crystal skeleton with a one-step chemical process. The exposed crystal plane enriches a large number of P–O– functional groups, affiniting with positively charged nuclide ions and efficiently for the U(VI) adsorption. In order to investigate the outstanding characteristics of 2D ultra-thin iron phosphate materials, three morphologies of iron phosphate (two-dimensional nanosheets, disks and octahedrons) were examined and optimized by comparing their adsorption capacities of uranyl ions. Additionally, the effects of pH, ionic strength and temperature on the adsorption behaviors were symmetrically analyzed. Along with the detailed characterization analysis, the possible adsorption and stacking mechanism between U(VI) and ultra-thin iron phosphate materials was discussed as well.

2. Experimental

2.1. Materials and Characterization methods

Cetyltrimethyl Ammonium Bromide (CTAB), Diethylene glycol (DG), $Fe(NO_3)_3 \cdot 9H_2O$, H_3PO_4, were obtained from Tianjin regent chemicals Co., Ltd (Tianjin, China, ≥99.0%), Shanghai Macklin Biochemical Co., Ltd. (Shanghai, China, ≥98.0%), Tianjin basf chemical

Co., Ltd. (Tianjin, China, ≥98.5%), Laiyang Far Eastern Drum Manufacturing Co., Ltd (Yantai, China, ≥85%), respectively. All other reagents were analytical-reagent grade. The characterization methods were illustrated in supplementary material.

2.2. Synthesis of iron phosphate samples

$Fe(NO_3)_3 \cdot 9H_2O$ (1.0100 g) and H_3PO_4 (0.40 mL) were dissolved in 50.00 mL DG by magnetic stirring, then CTAB (0.0101 g) was also dissolved the above transparent solution by magnetic stirring. The mixture solution was transferred into a 150 mL boiling flask-3-neck, heated to 200 ˚C in a sand bath magnetic stirring instrument (SZCL-A, 6˚C/min) and kept warm for 4 hours. The product was then separated by centrifugation and rinsed with acetone for 6–7 times, precipitates were finally collected by vacuum drying (85 ˚C, vacuum degree ＜ 0.09, 8 h). This sample was marked as FP1. FP 2 and 3 were prepared in the same method as FP1. The preparation amounts and conditions were listed in Table S1.

2.3. Batch adsorption experiments

Adsorption experiments were performed using batch technique in 10 mL polyethylene tubes. Proper sample suspension (0.2 $g \cdot L^{-1}$), $NaNO_3$ (0.001-0.1 $mol \cdot L^{-1}$) and U(VI) standard solutions (60 $mg \cdot L^{-1}$) were added into the above tubes to achieve the requirements of different adsorption experiments. The required pH value was adjusted by adding homemade 0.1 or 0.01$mol \cdot L^{-1}$ NaOH or HNO_3. To ensure adsorption equilibrium, the suspension was shaken for 24 h. According to Arsenazo III spectrophotometric method, the concentration of U(VI) was obtained at a wavelength of 669 nm. The adsorption capacities of U(VI) by FP1–3 were calculated as follows:

$$q_e = \frac{(C_0 - C_e)}{m} \times V \quad (1)$$

$$K_d = \frac{(C_0 - C_e)}{C_e} \times \frac{V}{m} \quad (2)$$

Where C_0 ($mg \cdot L^{-1}$) and C_e ($mg \cdot L^{-1}$) represent concentrations of U(VI) at initial and equilibrium time, respectively; V (L) and m (g) represent the volume of adsorption system and amount of FP1–3, respectively. All experimental data were average values of the triplicate determinations.

3. Results and Discussion

3.1. Characterization of iron phosphate samples

As shown in Fig. 2, the experimental XRD patterns of FP1 and FP2 match with the single crystal data of $Fe_7(PO_4)_6$ (ICSD#20765, a=6.314Å, b=7.967Å, c=9.546Å, P-1(2)) [64], whereas FP3 matches with $Fe_{2.95}(PO_4)_2(OH)_2$ (JCPDS#84-1912, a=7.310Å, b=7.310Å, c= 13.212Å). The morphology of samples was further characterized by FESEM and TEM (Fig. 3). From the FESEM and TEM images of FP1 (Fig. 3A and 3D), FP1 shows an ultra-thin two-dimensional morphology, which is in line with the triclinic P-1(2) without any high symmetry. Additionally, FP2 has a varying morphology form of disks, and some disks also stack or interlace together (Fig. 3B and 3E). And FP3 shows similar size form of octahedrons (Fig. 3C and 3F). Those results indicate that different morphology of iron phosphates can be successfully prepared with an easy organic solvent refluxing method and their phases change on the high concentrations of reactants.

Fig. 4 shows the AFM and HRTEM images of FP1 sheet sample. The AFM images of FP1 (Fig. 4A) indicate that the thickness of FP1 can reach 13-15 nm. In HRTEM of FP1 (Fig.

4B), the selected area electron diffraction (SAED) of ultra-thin FP1 sample shows both diffraction halo and diffraction spots. It indicates that the multilayer nanosheets in the view are made up of non aligned stacking of ordered nanocrystalline sheets. The disordered stacking leads to diffraction haloes, and the ordered nano sheets in the layers form diffraction spots. According to the radius calculation of the diffraction halo, the corresponding d value between those parallel crystal planes is 0.2984 nm, which is in good agreement with the d value of the strongest peak of $(0\bar{2}1)$ (0.2986 nm) in the ICSD#20765 standard XRD spectrum, and then the diffraction spots in the diffraction halo can be attributed to $(0\bar{2}1)$ crystal plane.

Fig. 5A, 5B and 5C show the adsorption-desorption curves and the pore size distributions (insets) of FP1-3, respectively. The unified results were listed in Table S2. FP1 possesses the relative highest specific surface areas (27.77 $m^2 \cdot g^{-1}$) and the smallest average pore diameters (8.45 nm), followed by 3.97 $m^2 \cdot g^{-1}$, 18.66 nm and 1.65 $m^2 \cdot g^{-1}$, 19.01 nm for FP2 and FP3, respectively. Compared the different adsorption-desorption curves of FP1-3, it is obvious that FP1 owns an adsorption hysteresis loop, suggesting that FP1 has some mesoporous morphologies. As for the reason, some curled nanosheets can be found from the Fig. 3D, which may be caused the generation of mesoporous morphology.

Zeta potential is an important means of showing the stability of materials in solution [65]. In the pH range of 2−11, the zeta potentials of FP1−3 have the same trends (Fig. 5D), specifically, the positive zeta potentials of FP1−3 exhibit in relative low pH range (<4.2) and negative zeta potentials in relative high pH range (>4.2), which can be attributed to the proton desorption from materials surface with the increasing pH [65]. Additionally, compared with FP2 and FP3, the zeta potential curves of FP1 moves upwardly and the isoelectric point

near pH value of 4.2 for FP1, 3.5 for FP2, 3.4 for FP3. Considering the result of specific surface areas and the different morphologies of FP1−3, FP1 owns the largest specific surfaces, more active sorption groups may expose on the surface of the material, which can absorb more protons from the solution and increase the difficulty of proton desorption from solid surface. Similar experiment results were also reported in other researches [4, 65]. According to above results, the two-dimensional morphology of materials can obviously influence their original surface properties, those changes will improve the adsorption capacity of U(VI).

The balanced adsorption capacity of U(VI) by FP1−3 were shown in Fig. 6. Compared with FP2 (24.51 $mg \cdot g^{-1}$) and FP3 (10.91 $mg \cdot g^{-1}$), the maximum actual saturated adsorption capacity of FP1 (656.91 $mg \cdot g^{-1}$) has greatly improved, even higher than phosphate functionalized graphene oxide (251.7 $mg \cdot g^{-1}$), showing a great application prospect in the field of radioactive adsorption, also indicating that making the adsorbent a two-dimensional material will be benefit to improve its adsorption performance [65]. In order to further facilitate the application of FP1 in the field of radioactive adsorption, it is particularly important to understand its adsorption mechanism of U(VI). Thus, the following research will focus on the adsorption behavior of ultra-thin FP1 in detail.

3.2. Batch adsorption of U(VI) on ultra-thin FP1

3.2.1. Effect of pH and ionic strength

As many studies have been reported that the liquid solution pH values has an important affect in the adsorbent surface charge and the speciation of the adsorbate [1, 4, 40, 65-70]

In the pH range of 2.0−6.0, the adsorption capacity of U(VI) increases gradually as pH increased, but decreases gradually with the pH values from 6.0 to 9.0 (Fig. 7A). The relative

distribution of U(VI) species (Fig. 7B) and the surface properties of FP1(Fig. 5D) under the different pH values can explain this adsorption trend. It should be noted that the relative distribution of U(VI) species are obtained by using the Visual MINTEQ mode, and the detailed reference data are shown in Table S3. As previously mentioned, the isoelectric point near pH value (pH_{zpc}) was 4.2 for FP1, the overall trend Zeta-potential values of FP1 gradually decreased from +20 mv to −40 mv with the pH increasing. From the Fig. 7B, the dominant species of uranyl ion was UO_2^{2+} at pH 2.0–4.2 (pH_{zpc}), but the adsorption capacity still keep high (170.80 $mg \cdot g^{-1}$ at pH = 2.0, 337.35 $mg \cdot g^{-1}$ at pH = 4.0), indicating that the strong sorption between UO_2^{2+} and FP1, and the adsorption mechanism may be surface complexation or strong chemical sorption at pH < 4.2 [52]. The major U(VI) species were UO_2^{2+}, $UO_2(OH)^+$, $UO_2(OH)_2$ at pH 4.2–6.0, $UO_2(OH)^+$, $UO_2(OH)_2$, UO_2CO_3 at pH 6.0–7.0, UO_2CO_3 , $UO_2(CO_3)_2^{2-}$ and $UO_2(CO_3)_3^{4-}$ at pH 7.0–9.0, respectively [22, 36]. Therefore, the adsorption is also affected by electrostatic interaction at pH ＞ 4.2.

Additionally, the adsorption property of U(VI) weakly depend on the change of ionic strength (0.001, 0.01 and 0.1 $mol \cdot L^{-1}$ $NaNO_3$) at pH from 2.0 to 9.0 (Fig. 7A). Compared with the outer-sphere surface complexes and ion exchange, which are greatly affected by pH and ionic strength, inner-sphere surface complexes are only depended on pH [36, 71]. Therefore, the adsorption mechanism of U(VI) by FP1 is likely an inner-sphere surface complexation mechanism. Some phosphate adsorbents (ZrP_2O_7 [38], $LaPO_4$ [37], $Fe_4(P_2O_7)_3$ [36] and PGO [40] also showed similar adsorption result of U(VI).

3.2.2. Adsorption kinetics

Adsorption kinetics is an important method to effectively reflect the adsorption

mechanism of adsorbates on materials [2, 72-74]. Results of adsorption kinetic experiments of U(VI) were shown in Fig. 8A, the adsorption capacity has an relatively fast adsorption equilibrium within 2h, then increases slightly with the adsorption time increasing, suggesting that the adsorption of U (VI) by FP1 is likely to be chemisorption [13, 40, 75, 76]. As shown in Fig. 8A, 8B and 8C, three adsorption kinetic models (pseudo-first-order kinetic, pseudo-second-order kinetic and intra-particle diffusion model) were applied to simulate the kinetic adsorption data and analyze the adsorption process. Their corresponding equations are as follows [4, 33, 77, 78]:

$$\ln(q_e - q_t) = \ln q_e - k_1 t \tag{3}$$

$$\frac{t}{q_t} = \frac{1}{k_2 q_e^{\,2}} + \frac{t}{q_e} \tag{4}$$

$$q_t = k_i t^{1/2} + C \tag{5}$$

Where q_e have been described earlier, q_t ($mg \cdot g^{-1}$) represents the adsorption capacity of U(VI) at different contact time t (h). The k_1 (h^{-1}), k_2 ($g \cdot mg^{-1} \cdot h^{-1}$) and k_i are the rate constant of pseudo-first-order, pseudo-second-order and intra-particle diffusion model adsorption, respectively. The results were shown in Table 1. Based on the higher R^2 (0.999 versus 0.946), pseudo-second-order model fits the adsorption kinetics curve very well, which also indicates that the adsorption mechanism of U(VI) onto FP1 is a chemisorption mechanism [77]. Compared with the maximum equilibrium adsorption capacity (q_{max} = 424.162 $mg \cdot g^{-1}$) of the pseudo-first-order model, the q_{max} of the pseudo-second-order model (431.034 $mg \cdot g^{-1}$) is closer to the actual measured value (431.999 $mg \cdot g^{-1}$), which provides a further evidence that pseudo-second-order model is more suitable to describe the kinetic adsorption processes [73].

Fig. 8C showed a multilinear relation between q_t and $t^{1/2}$, and the intercept of the simulated lines were also not zero, suggested the adsorption of U(VI) by FP1 was controlled by multiple factors [4, 33]. The first and second simulated lines describe that U(VI) diffuse to the surfaces and pores of FP1 in the solution, respectively. The final simulated line manifests the adsorption equilibrium progress, the reason attributes to the low concentration of U(VI) and the reduction of active sorption sites [4, 5, 22, 36, 72]. As shown in Table 1, K_{int1}(467.318 $mg \cdot g^{-1} \cdot h^{-0.5}$) is closer to the actual adsorption equilibrium value (431.999 $mg \cdot g^{-1}$) and higher than K_{int2}(98.446 $mg \cdot g^{-1} \cdot h^{-0.5}$) and K_{int3}(2.338 $mg \cdot g^{-1} \cdot h^{-0.5}$), showing the first factor plays the most important role in the adsorption process, and the second and third influencing factors decreased in turn. According to the above analysis, the active sites on the material surface has a more important role in the adsorption process than the pores, which is also consistent with the morphological characters of FP1 (fewer curled nanosheets and more two-dimensional nanosheets) in Fig. 3D.

3.2.3. Adsorption isotherms

The adsorption isotherms of U (VI) on FP1 were shown in Fig. 9A. It is clear that the adsorption capacity increases with the initial U(VI) concentration increasing, indicates that the initial U(VI) concentration has an important role in the mass transfer resistance of U(VI) between the liquid and solid phase [4, 79, 80].

Two frequently used isothermal models (Langmuir and Freundlich) were applied to simulate the adsorption date (Fig. 9B and 9C). The results of fitting data were listed in the Table 2. The Langmuir isothermal model is often used to describe monolayer adsorption, where adsorption activation energy is uniform on the adsorbent surface, and there is no

interaction between the adsorbates on adjacent sites, which can be defined as equation (6) [2, 8, 80]:

$$\frac{C_e}{q_e} = \frac{1}{q_{max} b} + \frac{C_e}{q_{max}} \quad (6)$$

$$R_L = \frac{1}{1 + bC_0} \quad (7)$$

Where C_0, C_e and q_e have been described earlier, b ($L.g^{-1}$) and q_{max} ($mg.g^{-1}$) are the Langmuir constant and the maximum adsorption capacity, respectively. Moreover, that the adsorption system is favorable or unfavorable can be determined by the quilibrium parameter (R_L), favorable ($0 < R_L < 1$) and unfavorable ($R_L > 1$) [81, 82]. Therefore, the adsorption system is favorable in this study ($R_{L\ 298\ K} = 0.076$, $R_{L\ 308\ K} = 0.062$, $R_{L\ 318\ K} = 0.058$).

The Freundlich isotherm model was used to describe the adsorption onto heterogenous surfaces [2, 40, 79]. The model can be defined as equation (8):

$$\log q_e = \log K_F + n \log C_e \quad (8)$$

Where K_F and n are Freundlich constants and indicate the adsorption capacity and adsorption intensity, respectively. Comparing the linear regression coefficient of the two isotherm models, the adsorption isotherms is more in line with the Langmuir model, suggesting a monolayer adsorption of U(VI) onto FP1 surfaces [2, 8, 35].

This monolayer adsorption result shows a close correspondence relationship with the two-dimensional morphology, many studies using two-dimensional materials for adsorbing U(VI) also have the same results [20, 40, 51, 62, 82, 83].

Additionally, it has been clearly shown that the adsorption capacity improve rapidly with the increasing temperature, which is also consistent with the changes of the equilibrium

parameter (R_L) with temperature ($R_{L\ 298\ K}$ = 0.076 ＞ $R_{L\ 308\ K}$ = 0.062 ＞ $R_{L\ 318\ K}$ = 0.058). As shown in Table 3, FP1 shows an excellent adsorption capacity (704.23 $mg \cdot g^{-1}$). This also makes it a promising material for adsorbing U(VI) in wastewater disposal when compared with most two-dimensional materials (MgFeAl-LDHs [82], Phosphonate and carboxylic acid co-functionalized MoS_2 sheets [51], PGO [40] and Ozonated GO [20]), block phosphate adsorbents (ZrP_2O_7 [38], $Al_4(P_2O_7)_3$ [22], $Fe_4(P_2O_7)_3$ [36]) organic phosphate adsorbents (Chitosan-tripolyphosphate [33], Phosphorus-modified chelating resin [34], Phosphoryl functionalized SiO_2 [35]) and some adsorbents ($MnFe_2O_4$ [84], Perovskite [70], Polypyrrole [85], Pyrrhotite [86]).

3.2.4. Adsorption thermodynamics

To gain a deep understanding of the role of temperature in this adsorption process, the thermodynamic parameters including standard enthalpy change (ΔH^0), standard Gibbs free energy change (ΔG^0) and entropy change (ΔS^0) for U(VI) adsorption on FP1 were calculated from the following equations (9) and (10) [36, 65, 84, 87, 88]:

$$\Delta G^0 = -RT \ln K^0 \tag{9}$$

$$\ln K^0 = \frac{\Delta S^0}{R} - \frac{\Delta H^0}{RT} \tag{10}$$

Where K^0 is the adsorption equilibrium constant, and R (8.314 $J \cdot mol^{-1} \cdot K^{-1}$) is the ideal gas constant [22, 36]. According to the equations (9) and (10), the specific calculation process and relationship curves were shown in Fig. 10.

The results of adsorption thermodynamics were calculated and listed in Table 4. The ΔH^0 (16.57 $KJ \cdot mol^{-1}$) and negative ΔG^0 values indicate that the adsorption process of U(VI) by

FP1 is an endothermic and spontaneous process. According to the changes of ΔG^0 with temperature, the elevated temperature will be beneficial to the adsorption of U(VI) by FP1. The positive ΔS^0 (91.01 $J \cdot mol^{-1} \cdot K^{-1}$) reflects the strong interaction between FP1 and U(VI), which also indicates that some possible structural or morphological changes in FP1 during the adsorption process [1, 40].

3.3. Possible adsorption mechanism

When comparing the morphology changes of FP1 before and after adsorption (Fig. 11A and 11C), it was clear that the distribution of FP1 is relatively concentrated. Further magnification (Fig. 11B and 11D) of FP1 have an obvious accumulation and agglomeration phenomenon after adsorption. A large number of two-dimensional nanosheets stack and reorganize into a large aggregate. Additionally, the adsorbed samples were analyzed by EDS and Mapping (Fig. 11F and 11G), the content of U on the samples surface after adsorption is very low (0.14%), which is contradictory to the high adsorption. EDS and Mapping only analyze the elements on the surface of the material, and the detection depth is limited [82, 89]. Considering the thickness of the FP1 nanosheets (＞13 nm) and the obvious agglomeration phenomenon after adsorption, we speculate that the addition of U(VI) will make the two-dimensional nanosheets stacked, and then the agglomeration phenomenon of FP1 nanosheets after adsorption impedes the detection of U by EDS and Mapping.

The FT-IR of FP1 before and after the adsorption was shown in Fig. 12. The observed bands of 1632 and 3421 cm^{-1} could be regarded as the bending and stretching vibrations of absorbed water, respectively. The observed bands of 545 cm^{-1} and 1076 cm^{-1} were attributed

to the symmetric stretching and asymmetric stretching vibration modes of P–O in phosphate group, respectively. The observed band of 1245 cm^{-1} could be regarded as asymmetric stretching vibration modes of P=O [33-35, 88-91]. Compared the difference between the before and after adsorption peak position of FP1, the new peak of the antisymmetric stretching vibration modes of O=U=O appeared at 923 cm^{-1} [92-96]. The peak position of P=O moved to the right, from 1245 to 1235 cm^{-1} and the peak position of P–O had the similar changes, from 1076 to 1003 cm^{-1}, 545 to 535 cm^{-1}, respectively. All results indicated that U(VI) adsorbed on the two-dimensional surface of FP1, and then it brought about the change of phosphorus oxygen bonds [92-96]. As shown in the Fig. S1, the XRD patterns are well maintained after sorption, indicating that the crystal structures of FP1 have not suffered any significant destruction. Besides, no additional diffraction peaks appears in the XRD pattern of FP1 after adsorption, indicating that the adsorbed U(VI) species are not crystallized. Hence, the change of adsorption process mostly occurs in the apparent morphology but not in the internal structure.

Based on the above analysis results, the possible adsorption progress of U(VI) by FP1 was shown in Fig. 13. Due to the strong monolayer complexation between phosphate group and U(VI), U(VI) adsorbs on the surface of FP1, forming an inner-sphere surface complexes. Meanwhile, U(VI) can be used as a connecting ion to connect FP1 nanosheets. The FP1 nanosheets then continuously stack together until they finally form a stacked aggregation, which causes the U(VI) to become trapped between the nanosheets of FP1. Obviously, this adsorption mode of monolayer surface complexation and stacking (it was called as MSCS-Mode by our group) between ultra-thin FP1 nanosheets and U (VI) also could provide

a meaningful adsorption mechanism for other nanosheet adsorbents in the treatment of radioactive wastewater.

4. Conclusion

In this study, the ultra-thin two-dimensional iron phosphate ($Fe_7(PO_4)_6$) nanosheets was synthesized by using an one-step solvent refluxing method. The morphologies and phases of the samples could be fine-adjusted by the initial reactant concentrations. Compared with either conversional phosphate adsorbents and current reported 2D U(VI) adsorbents, FP1 shows a higher adsorption capacity (704.23 $mg \cdot g^{-1}$ at 298 K), which is about 27 times of conventional 3D $Fe_7(PO_4)_6$ (24.51 $mg \cdot g^{-1}$-sample FP2) and 2 times higher than phosphate functionalized graphene oxide (251.7 $mg \cdot g^{-1}$). Obviously, through changing the morphology of $Fe_7(PO_4)_6$ to be two-dimensional, its adsorption performance are greatly improved. Consistent with conventional U(VI) adsorbents, the pH, Zeta potential, specific surface area and average pore diameter have positive impact to this adsorption. But the effect from ionic strength is negligible, which is similar with other phosphate adsorbents. With the results of adsorption tests and the systematic characterizations of FESEM, EDS and Mapping after adsorption, the adsorption of U(VI) onto FP1 is considered as a relatively rapid, spontaneous and endothermic process, and following a monolayer surface complexation and stacking mode (MSCS-Mode), which ensure the high accessibility and efficiency of adsorption.

In summary, this preparation method could be generalized to the preparation of other two-dimensional phosphate materials, and the novel adsorption mechanism (MSCS-Mode) study also provides a new clue for the study of other two-dimensional adsorption materials.

Acknowledgement

This research was financially supported by the Science and Technology Development Plan (NO. J17KA006) from Shandong Provincial Education Department， the Key Program for Basic Research of Natural Science Foundation (ZR2018ZC0946) of Shandong Province and the National Natural Science Foundation of China (No. 51673090, 51173074). The authors acknowledge the supports from the NIMHD-RCMI (5G12MD007595), NIGMS-BUILD (5UL1GM118967-05) and National Science Foundation (Grant HRD-1700429 and CHE-1832167).

References

[1] Y.N. Wang, H.Y. Huang, S.X. Duan, X. Liu, J. Sun, T. Hayat, A. Alsaedi, J.X. Li, A New Application of a Mesoporous Hybrid of Tungsten Oxide and Carbon as an Adsorbent for Elimination of Sr^{2+} and Co^{2+} from an Aquatic Environment, ACS Sustainable Chem. Eng. 6 (2018) 2462-2473.

[2] D.Z. Yuan, L. Chen, X. Xiong, L.G. Yuan, S.J. Liao, Y. Wang, Removal of uranium (VI) from aqueous solution by amidoxime functionalized superparamagnetic polymer microspheres prepared by a controlled radical polymerization in the presence of DPE, Chem. Eng. J. 285 (2016) 358-367.

[3] W.M. Alley, R. Alley, The growing problem of stranded used nuclear fuel, Environ. Sci. Technol. 48 (2014) 2091-2096.

[4] S.X. Duan, Y.N. Wang, X. Liu, D.D. Shao, T. Hayat, A. Alsaedi, J.X. Li, Removal of U(VI) from Aqueous Solution by Amino Functionalized Flake Graphite Prepared by Plasma Treatment, ACS Sustainable Chem. Eng. 5 (2017) 4073-4085.

[5] Y.G. Zhao, X.X. Wang, J.X. Li, X.K. Wang, Amidoxime functionalization of mesoporous silica and its high removal of U(vi), Polym. Chem. 6 (2015) 5376-5384.

[6] A. Mellah, S. Chegrouche, M. Barkat, The precipitation of ammonium uranyl carbonate (AUC): Thermodynamic and kinetic investigations, Hydrometallurgy, 85 (2007) 163-171.

[7] D.J. Rokop, R.E. Perrin, G.W. Knobeloch, V.M. Armijo, W.R. Shields, Thermal Ionization Mass Spectrometry of Uranium with Electrodeposition as a Loading Technique, Anal. Chem. 54 (1982) 957-960.

[8] M.L. Feng, D. Sarma, X.H. Qi, K.Z. Du, X.Y. Huang, M.G. Kanatzidis, Efficient Removal and Recovery of Uranium by a Layered Organic-Inorganic Hybrid

Thiostannate, J. Am. Chem. Soc. 138 (2016) 12578-12585.

[9] N. Kabay, M. Demircioğlu, S. Yaylı, E. Günay, M. Yüksel, M. Sağllam, M. Streat, Recovery of Uranium from Phosphoric Acid Solutions Using Chelating Ion-Exchange Resins, Ind. Eng. Chem. Res. 37 (1998) 1983-1990.

[10] Z.Z. Pan, W.L. Li, J.D. Fortner, D.E. Giammar, Measurement and Surface Complexation Modeling of U(VI) Adsorption to Engineered Iron Oxide Nanoparticles, Environ. Sci. Technol. 51 (2017) 9219-9226.

[11] D.D. Shao, G.S. Hou, J.X. Li, T. Wen, X.M. Ren, X.K. Wang, PANI/GO as a super adsorbent for the selective adsorption of uranium(VI), Chem. Eng. J. 255 (2014) 604-612.

[12] X.X. Wang, J.X. Li, S.Y. Dai, T. Hayat, A. Alsaedi, X.K. Wang, Interactions of Eu(III) and ^{243}Am(III) with humic acid-bound γ-Al_2O_3 studied using batch and kinetic dissociation techniques, Chem. Eng. J. 273 (2015) 588-594.

[13] Z.W. Zhao, J.X. Li, T. Wen, C.C. Shen, X.K. Wang, A.W. Xu, Surface functionalization graphene oxide by polydopamine for high affinity of radionuclides, Colloids and Surfaces A: Physicochem. Eng. Aspects, 482 (2015) 258-266.

[14] Y.B. Sun, D.D. Shao, C.L. Chen, S.B. Yang, X.K. Wang, Highly efficient enrichment of radionuclides on graphene oxide-supported polyaniline, Environ. Sci. Technol. 47 (2013) 9904-9910.

[15] Y.B. Sun, S.B. Yang, Y. Chen, C.C. Ding, W.C. Cheng, X.K. Wang, Adsorption and desorption of U(VI) on functionalized graphene oxides: a combined experimental and theoretical study, Environ. Sci. Technol. 49 (2015) 4255-4262.

[16] Y.B. Sun, Z.Y. Wu, X.X. Wang, C.C. Ding, W.C. Cheng, S.H. Yu, X.K. Wang, Macroscopic and Microscopic Investigation of U(VI) and Eu(III) Adsorption on Carbonaceous Nanofibers, Environ. Sci. Technol. 50 (2016) 4459-4467.

[17] Y.B. Sun, S.H. Lu, X.X. Wang, C. Xu, J.X. Li, C.L. Chen, J. Chen, T. Hayat, A. Alsaedi, N.S. Alharbi, X.K. Wang, Plasma-Facilitated Synthesis of Amidoxime/Carbon Nanofiber Hybrids for Effective Enrichment of $^{(238)}$U(VI) and $^{(241)}$Am(III), Environ. Sci. Technol. 51 (2017) 12274-12282.

[18] A.J.C. Semião, H.M.A. Rossiter, A.I. Schäfer, Impact of organic matter and speciation on the behaviour of uranium in submerged ultrafiltration, J. Membrane Sci. 348 (2010) 174-180.

[19] X. Liu, Y.S. Huang, S.X. Duan, Y.N. Wang, J.X. Li, Y.T. Chen, T. Hayat, X.K. Wang, Graphene oxides with different oxidation degrees for Co(II) ion pollution management, Chem. Eng. J. 302 (2016) 763-772.

[20] X. Liu, X.X. Wang, J.X. Li, X.K. Wang, Ozonated graphene oxides as high efficient sorbents for Sr(II) and U(VI) removal from aqueous solutions, Sci. China Chem. 59 (2016) 869-877.

[21] Y.N. Wang, X. Liu, Y.S. Huang, T. Hayat, A. Alsaedi, J.X. Li, Interaction mechanisms of U(VI) and graphene oxide from the perspective of particle size distribution, J. Radioanal. Nucl. Chem. 311 (2017) 209-217.

[22] D. Wang, Y.B. Xu, L.X. Yang, F. Wang, A.M. Asiri, K.A. Alamry, Synthesis of aluminum pyrophosphate for efficient sorption of U(VI), J. Mol. Liq. 258 (2018) 327-334.

[23] J. Li, X.X. Wang, G.X. Zhao, C.L. Chen, Z.F. Chai, A. Alsaedi, T. Hayat, X.K. Wang, Metal-organic framework-based materials: superior adsorbents for the capture of toxic and radioactive metal ions, Chem. Soc. Rev. 47 (2018) 2322-2356.

[24] S. Song, S. Zhang, S.Y. Huang, R. Zhang, L. Yin, Y.Z. Hu, T. Wen, L. Zhuang, B.W. Hu, X.K. Wang, A novel multi-shelled Fe_3O_4@MnO_x hollow microspheres for immobilizing U(VI) and Eu(III), Chem. Eng. J. 355 (2019) 697-709.

[25] L. Yin, S. Song, X.X. Wang, F.L. Niu, R. Ma, S.J. Yu, T. Wen, Y.T. Chen, T. Hayat, A. Alsaedi, X.K. Wang, Rationally designed core-shell and yolk-shell magnetic titanate nanosheets for efficient U(VI) adsorption performance, Environ. Pollut. 238 (2018) 725-738.

[26] G.X. Zhao, X.B. Huang, Z.W. Tang, Q.F. Huang, F.L. Niu, X.K. Wang, Polymer-based nanocomposites for heavy metal ions removal from aqueous solution: a review, Polym. Chem. 9 (2018) 3562-3582.

[27] P. Bénard-Rocherulél, M. Louër, D. Louër, N. Dacheux, V. Brandel, M. Genet, Structure Determination of Uranium Halogenide Phosphates $UXPO_4 \cdot 2H_2O$(Cl, Br) from Powder Diffraction Date, J. Solid State Chem. 132 (1997) 315-322.

[28] I. Bonhoure, S. Meca, V. Marti, J.D. Pablo, J.L. Cortina, A new time-resolved laser-induced fluorescence spectrometry (TRLFS) data acquisition procedure applied to the uranyl- phosphate system, Radiochim. Acta, 95 (2007) 165-172.

[29] J. Crea, R. Digiusto, S.F. Lincoln, E.H. Williams, A Nuclear Magnetic Resonance Study of Ligand Exchange on Dioxopentakis(trimethyl phosphate) uranium (VI) Ion and Its Triethyl Phosphate Analogue, Inorg. Chem. 16 (1977) 2825-2829.

[30] N. Dacheux, N. Clavier, A.C. Robisson, O. Terra, F. Audubert, J.É. Lartigue, C. Guy, Immobilisation of actinides in phosphate matrices, C. R. Chimie, 7 (2004) 1141-1152.

[31] A. Kirishima, T. Kimura, O. Tochiyama, Z. Yoshida, Speciation study on complex formation of uranium(VI) with phosphate and fluoride at high temperatures and pressures by time-resolved laser-induced fluorescence spectroscopy, Radiochim. Acta, 92 (2004) 889-896.

[32] L. Lu, F. Chen, R.C. Ewing, R. Wang, Trace element immobilization by uranyl minerals in granite-hosted uranium ores: Evidences from the Xiazhuang ore field of Guangdong province, China, Radiochim. Acta, 95 (2007) 25-32.

[33] M.K. Sureshkumar, D. Das, M.B. Mallia, P.C. Gupta, Adsorption of uranium from aqueous solution using chitosan-tripolyphosphate (CTPP) beads, J. Hazard. Mater. 184 (2010) 65-72.

[34] Q. Cao, Y.C. Liu, C.Z. Wang, J.S. Cheng, Phosphorus-modified poly (styrene-co-divinylbenzene)-PAMAM chelating resin for the adsorption of uranium(VI) in aqueous, J. Hazard. Mater. 263 (2013) 311-321.

[35] X. Guo, Y.R. Feng, L. Ma, D.Z. Gao, J. Jing, J.C. Yu, H.B. Sun, H.Y. Gong, Y.J. Zhang, Phosphoryl functionalized mesoporous silica for uranium adsorption, Appl. Surf. Sci. 402 (2017) 53-60.

[36] X. Liu, Y.B. Xu, R.C. Jin, P. Yin, L.X. Sun, T. Liang, S.M. Gao, Facile synthesis of hierarchical $Fe_4(P_2O_7)_3$ for removal of U(VI), J. Mol. Liq. 200 (2014) 311-318.

[37] E. Ordoñez-Regil, R. Drot, E. Simoni, Surface complexation modeling of uranium(VI)

sorbed onto lanthanum monophosphate, J. Colloid Interf. Sci. 263 (2003) 391-399.
[38] L.J. Qian, P.Z. Hu, Z.J. Jiang, Y.X. Geng, W.S. Wu, Effect of pH, fulvic acid and temperature on the sorption of uranyl on ZrP_2O_7, Sci. China Chem. 53 (2010) 1429-1437.
[39] R. Drot, E. Simoni, M. Alnot, J.J. Ehrhardt, Structural Environment of Uranium (VI) and Europium (III) Species Sorbed onto Phosphate Surfaces: XPS and Optical Spectroscopy Studies, J. Colloid Interf. Sci. 205 (1998) 410-416.
[40] X. Liu, J.X. Li, X.X. Wang, C.L. Chen, X.K. Wang, High performance of phosphate-functionalized graphene oxide for the selective adsorption of U(VI) from acidic solution, J. Nucl. Mater. 466 (2015) 56-64.
[41] J.M.M. Millet, FePO Catalysts for the Selective Oxidative Dehydrogenation of Isobutyric Acid into Methacrylic Acid, Catal. Rev. 40 (1998) 1-38.
[42] M.G. Mesko, D.E. Day, B.C. Bunker, Immobilization of CsCl and SrF_2 in iron phosphate glass, Waste Manage. 20 (2000) 271-278.
[43] V. Lenoble, C. Laclautre, V. Deluchat, B. Serpaud, J.C. Bollinger, Arsenic removal by adsorption on iron(III) phosphate, J. Hazard. Mater. 123 (2005) 262-268.
[44] X.X. Zhang, C.L. Sun, L. Zhang, H. Liu, B.X. Cao, L.B. Liu, W.M. Gong, Adsorption studies of cadmium onto magnetic Fe_3O_4@$FePO_4$ and its preconcentration with detection by electrothermal atomic absorption spectrometry, Talanta, 181 (2018) 352-358.
[45] K. Zaghib, C.M. Julien, Structure and electrochemistry of $FePO_4 \cdot 2H_2O$ hydrate, J. Power Sources, 142 (2005) 279-284.
[46] J. Santos-Peña, P. Soudan, C.O. Areán, G.T. Palomino, S. Franger, Electrochemical properties of mesoporous iron phosphate in lithium batteries, J. Solid State Electr. 10 (2006) 1-9.
[47] M.C. Duff, J.U. Coughlin, D.B. Hunter, Uranium co-precipitation with iron oxide minerals, Geochim. Cosmochim. AC. 66 (2002) 3533-3547.
[48] J.K. Fredrickson, J.M. Zachara, D.W. Kednedy, M.C. Duff, Y.A. Gorby, S.W. Li, K.M. Krupka, Reduction of U(VI) in goethite (a-FeOOH) suspensions by a dissimilatory metal-reducing bacterium, Geochim. Cosmochim. AC. 64 (2000) 3085-3098.
[49] A.L. Yang, Y.K. Zhu, C.P. Huang, Facile preparation and adsorption performance of graphene oxide-manganese oxide composite for uranium, Sci. Rep. 8 (2018) 9058.
[50] Y.J. Zhang, J.H. Lan, L. Wang, Q.Y. Wu, C.Z. Wang, T. Bo, Z.F. Chai, W.Q. Shi, Adsorption of uranyl species on hydroxylated titanium carbide nanosheet: A first-principles study, J. Hazard. Mater. 308 (2016) 402-410.
[51] S. Yang, M.X. Hua, L. Shen, X.L. Han, M.Y. Xu, L.J. Kuang, D.B. Hua, Phosphonate and carboxylic acid co-functionalized MoS_2 sheets for efficient sorption of uranium and europium: Multiple groups for broad-spectrum adsorption, J. Hazard. Mater. 354 (2018) 191- 197.
[52] L. Yin, Y.Z. Hu, R. Ma, T. Wen, X.X. Wang, B.W. Hu, Z.M. Yu, T. Hayat, A. Alsaedi, X.K. Wang, Smart construction of mesoporous carbon templated hierarchical Mg-Al and Ni-Al layered double hydroxides for remarkably enhanced U(VI) management, Chem. Eng. J. 359 (2019) 1550-1562.
[53] P.C. Gu, S. Zhang, X. Li, X.X. Wang, T. Wen, R. Jehan, A. Alsaedi, T. Hayat, X.K. Wang,

Recent advances in layered double hydroxide-based nanomaterials for the removal of radionuclides from aqueous solution, Environ. Pollut. 240 (2018) 493-505.
[54] K.K. Chang, Y.X. Sun, F. Ye, X. Li, G.D. Sheng, D.L. Zhao, W.S. Linghu, H. Li, J. Liu, Macroscopic and molecular study of the sorption and co-sorption of graphene oxide and Eu(III) onto layered double hydroxides, Chem. Eng. J. 325 (2017) 665-671.
[55] L.Z. Feng, Z. Liu, Graphene in biomedicine: opportunities and challenges, Nanomedicine, 6 (2011) 317-324.
[56] B.W. Hu, C.C. Huang, X. Li, G.D. Sheng, H. Li, X.M. Ren, J.Y. Ma, J. Wang, Y.Y. Huang, Macroscopic and spectroscopic insights into the mutual interaction of graphene oxide, Cu(II), and Mg/Al layered double hydroxides, Chem. Eng. J. 313 (2017) 527-534.
[57] C.W. Hua, Q. Wang, H.T. Zhao, L.Z. Wang, S.F. Guo, X.L. Li, Ecotoxicological effects of graphene oxide on the protozoan Euglena gracilis, Chemosphere, 128 (2015) 184-190.
[58] Z.W. Huang, Z.J. Li, L.R. Zheng, L.M. Zhou, Z.F. Chai, X.L. Wang, W.Q. Shi, Interaction mechanism of uranium(VI) with three-dimensional graphene oxide-chitosan composite: Insights from batch experiments, IR, XPS, and EXAFS spectroscopy, Chem. Eng. J. 328 (2017) 1066-1074.
[59] Z.J. Li, F. Chen, L.Y. Yuan, Y.L. Liu, Y.L. Zhao, Z.F. Chai, W.Q. Shi, Uranium(VI) adsorption on graphene oxide nanosheets from aqueous solutions, Chem. Eng. J. 210 (2012) 539-546.
[60] S.B. Liu, T.H. Zeng, M. Hofmann, E. Burcombe, J. Wei, R.R. Jiang, J. Kong, Y. Chen, Antibacterial Activity of Graphite, Graphite Oxide, Graphene Oxide, and Reduced Graphene Oxide: Membrane and Oxidative Stress, ACS. Nano, 5 (2011) 6971-6980.
[61] L. Mu, Y. Gao, X.G. Hu, L-cysteine: a biocompatible, breathable and beneficial coating for graphene oxide, Biomaterials, 52 (2015) 301-311.
[62] X.X. Wang, Q.H. Fan, S.J. Yu, Z.S. Chen, Y.J. Ai, Y.B. Sun, A. Hobiny, A. Alsaedi, X.K. Wang, High sorption of U(VI) on graphene oxides studied by batch experimental and theoretical calculations, Chem. Eng. J. 287 (2016) 448-455.
[63] Y.D. Zou, X.X. Wang, Y.J. Ai, Y.H. Liu, J.X. Li, Y.F. Ji, X.K. Wang, Coagulation Behavior of Graphene Oxide on Nanocrystallined Mg/Al Layered Double Hydroxides: Batch Experimental and Theoretical Calculation Study, Environ. Sci. Technol. 50 (2016) 3658-3667.
[64] E. Kozlyakova, I. Danilovich, A. Volkov, K. Zakharov, O. Dimitrova, E. Belokoneva, L. Shvanskaya, E. Zvereva, D. Chareev, O. Volkova, A. Vasiliev, Tuning of physical properties of $Fe_7(PO_4)_6$ by sodium intercalation, J. Alloy. Compd. 744 (2018) 600-605.
[65] H. Xu, B.S. Zhu, X.M. Ren, D.D. Shao, X.L. Tan, C.L. Chen, Controlled synthesized natroalunite microtubes applied for cadmium(II) and phosphate co-removal, J. Hazard. Mater. 314 (2016) 249-259.
[66] H.B. Liu, M.X. Li, T.H. Chen, C.L. Chen, N.S. Alharbi, T. Hayat, D. Chen, Q. Zhang, Y.B. Sun, New Synthesis of nZVI/C Composites as an Efficient Adsorbent for the Uptake of U(VI) from Aqueous Solutions, Environ. Sci. Technol. 51 (2017) 9227-9234.
[67] Y.B. Sun, J.H. Lan, M.X. Li, W. Hu, H.B. Liu, G. Song, D.Y. Chen, W.Q. Shi, X.K. Wang, Influence of aqueous sulfide on speciation of U(vi) adsorbed to nanomagnetite, Environ. Sci.: Nano, 5 (2018) 1981-1989.

[68] T. Wan, W. Cheng, J.H. Ren, W. Wu, M. Wang, B.W. Hu, Z.Y. Jia, Y.B. Sun, The influence of nanoscale size on the adsorption–desorption of U(vi) on nano-Al oxides, Environ. Sci.: Nano, 5 (2018) 2731-2741.

[69] B.W. Hu, X.J. Guo, C. Zheng, G. Song, D.Y. Chen, Y.L. Zhu, X.F. Song, Y.B. Sun, Plasma-enhanced amidoxime/magnetic graphene oxide for efficient enrichment of U(VI) investigated by EXAFS and modeling techniques, Chem. Eng. J. 357 (2019) 66-74.

[70] S.H. Lu, K.R. Zhu, T. Hayat, N.S. Alharbi, C.L. Chen, G. Song, D.Y. Chen, Y.B. Sun, Influence of carbonate on sequestration of U(VI) on perovskite, J. Hazard. Mater. 364 (2019) 100-107.

[71] Y.B. Sun, Q. Wang, C.L. Chen, X.L. Tan, X.K. Wang, Interaction between Eu(III) and graphene oxide nanosheets investigated by batch and extended X-ray absorption fine structure spectroscopy and by modeling techniques, Environ. Sci. Technol. 46 (2012) 6020-6027.

[72] Y. Liu, L. Xu, J.S. Liu, X.Y. Liu, C.H. Chen, G.Y. Li, Y.F. Meng, Graphene oxides cross-linked with hyperbranched polyethylenimines: Preparation, characterization and their potential as recyclable and highly efficient adsorption materials for lead(II) ions, Chem. Eng. J. 285 (2016) 698-708.

[73] Y.Z. Niu, R.J. Qu, H. Chen, L. Mu, X.G. Liu, T. Wang, Y. Zhang, C.M. Sun, Synthesis of silica gel supported salicylaldehyde modified PAMAM dendrimers for the effective removal of Hg(II) from aqueous solution, J. Hazard. Mater. 278 (2014) 267-278.

[74] S.X. Zhang, Y.Y. Zhang, J.S. Liu, Q. Xu, H.Q. Xiao, X.Y. Wang, H. Xu, J. Zhou, Thiol modified Fe_3O_4@SiO_2 as a robust, high effective, and recycling magnetic sorbent for mercury removal, Chem. Eng. J. 226 (2013) 30-38.

[75] R. Hu, X.K. Wang, S.Y. Dai, D.D. Shao, T. Hayat, A. Alsaedi, Application of graphitic carbon nitride for the removal of Pb(II) and aniline from aqueous solutions, Chem. Eng. J. 260 (2015) 469-477.

[76] H.Y. Mei, X.L. Tan, S.J. Yu, X.M. Ren, C.L. Chen, X.K. Wang, Effect of silicate on U(VI) sorption to γ-Al_2O_3: Batch and EXAFS studies, Chem. Eng. J. 269 (2015) 371-378.

[77] Y.S. Ho, Review of second-order models for adsorption systems, J. Hazard. Mater. 136 (2006) 681-689.

[78] Y.F. Wang, R.J. Qu, F.W. Pan, X.H. Jia, C.M. Sun, C.N. Ji, Y. Zhang, K. An, Y.L. Mu, Preparation and characterization of thiol- and amino-functionalized polysilsesquioxane coated poly (p-phenylenetherephthal amide) fibers and their adsorption properties towards Hg(II), Chem. Eng. J. 317 (2017) 187-203.

[79] A. Günay, E. Arslankaya, İ. Tosun, Lead removal from aqueous solution by natural and pretreated clinoptilolite: adsorption equilibrium and kinetics, J. Hazard. Mater. 146 (2007) 362-371.

[80] C.T. Hsieh, H. Teng, Langmuir and Dubinin–Radushkevich analyses on equilibrium adsorption of activated carbon fabrics in aqueous solutions, J. Chem. Technol. Biotechnol. 75 (2000) 1066-1072.

[81] X. Liu, X.T. Xu, J. Sun, A. Alsaedi, T. Hayat, J.X. Li, X.K. Wang, Insight into the impact of interaction between attapulgite and graphene oxide on the adsorption of U(VI), Chem. Eng. J. 343 (2018) 217-224.

[82] S. Song, L. Yin, X.X. Wang, L. Liu, S.Y. Huang, R. Zhang, T. Wen, S.J. Yu, D. Fu, T. Hayat, X.K. Wang, Interaction of U(VI) with ternary layered double hydroxides by combined batch experiments and spectroscopy study, Chem. Eng. J. 338 (2018) 579-590.

[83] L. Wang, L.Y. Yuan, K. Chen, Y.J. Zhang, Q.H. Deng, S.Y. Du, Q. Huang, L.R. Zheng, J. Zhang, Z.F. Chai, M.W. Barsoum, X.K. Wang, W.Q. Shi, Loading Actinides in Multilayered Structures for Nuclear Waste Treatment: The First Case Study of Uranium Capture with Vanadium Carbide MXene, ACS Appl. Mater. Interfaces, 8 (2016) 16396-16403.

[84] Y.Z. Hu, C.F. Zhao, L. Yin, T. Wen, Y. Yang, Y.J. Ai, X.K. Wang, Combining batch technique with theoretical calculation studies to analyze the highly efficient enrichment of U(VI) and Eu(III) on magnetic $MnFe_2O_4$ nanocubes, Chem. Eng. J. 349 (2018) 347-357.

[85] S. Abdi, M. Nasiri, A. Mesbahi, M.H. Khani, Investigation of uranium (VI) adsorption by polypyrrole, J. Hazard. Mater. 332 (2017) 132-139.

[86] H.B. Liu, Y.K. Zhu, B. Xu, P. Li, Y.B. Sun, T.H. Chen, Mechanical investigation of U(VI) on pyrrhotite by batch, EXAFS and modeling techniques, J. Hazard. Mater. 322 (2017) 488- 498.

[87] J. Chen, R.J. Qu, Y. Zhang, C.M. Sun, C.H. Wang, C.N. Ji, P. Yin, H. Chen, Y.Z. Niu, Preparation of silica gel supported amidoxime adsorbents for selective adsorption of Hg(II) from aqueous solution, Chem. Eng. J. 209 (2012) 235-244.

[88] Y. Zhang, R.J. Qu, C.M. Sun, C.N. Ji, H. Chen, P. Yin, Improved synthesis of silica-gel-based dendrimer-like highly branched polymer as the Au(III) adsorbents, Chem. Eng. J. 270 (2015) 110-121.

[89] N.R. Lugg, G. Kothleitner, N. Shibata, Y. Ikuhara, On the quantitativeness of EDS STEM, Ultramicroscopy, 151 (2015) 150-159.

[90] S. Mustafa, A. Naeem, S.U. Nisa, S. Murtaza, M. Khalid, The Mechanism of Alkali Metal Ion Sorption by Iron(III) Phosphate, Adsorpt. Sci. Technol. 17 (1999) 715-727.

[91] L. Popović, D. de Waal, J.C.A. Boeyens, Correlation between Raman wavenumbers and P-O bond lengths in crystalline inorganic phosphates, J. Raman Spectrosc. 36 (2005) 2-11.

[92] A. Barkleit, H. Foerstendorf, B. Li, A. Rossberg, H. Moll, G. Bernhard, Coordination of uranium(VI) with functional groups of bacterial lipopolysaccharide studied by EXAFS and FT-IR spectroscopy, Dalton Trans. 40 (2011) 9868-9876.

[93] G. Lefevre, S. Noinville, M. Fédoroff, Study of uranyl sorption onto hematite by in situ attenuated total reflection-infrared spectroscopy, J. Colloid Interf. Sci. 296 (2006) 608-613.

[94] B. Li, J. Raff, A. Barkleit, G. Bernhard, H. Foerstendorf, Complexation of U(VI) with highly phosphorylated protein, phosvitin A vibrational spectroscopic approach, J. Inorg. Biochem. 104 (2010) 718-725.

[95] K. Müller, V. Brendler, H. Foerstendorf, Aqueous Uranium(VI) Hydrolysis Species Characterized by Attenuated Total Reflection Fourier-Transform Infrared Spectroscopy, Inorg. Chem. 47 (2008) 10127-10134.

[96] K. Vidya, V.S. Kamble, N.M. Gupta, P. Selvam, An in situ FT-IR study of photo-

oxidation of alcohols over uranyl-anchored MCM-41: Possible reaction pathways, J. Catal. 247 (2007) 1-19.

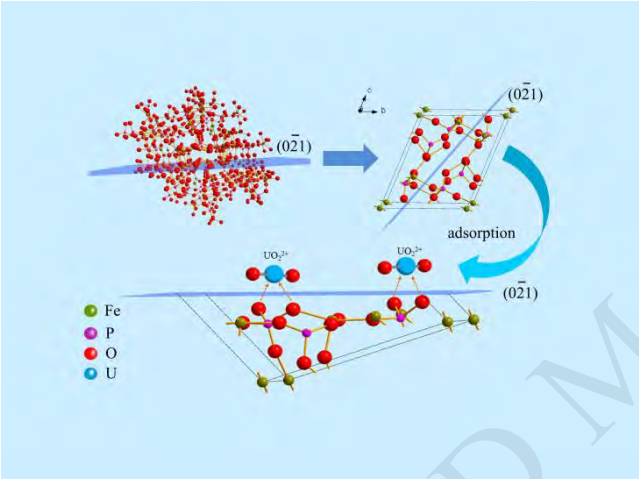

Figure 1. The tailor and adsorption fictitious mechanism of ultra-thin $Fe_7(PO_4)_6$ nanosheets.

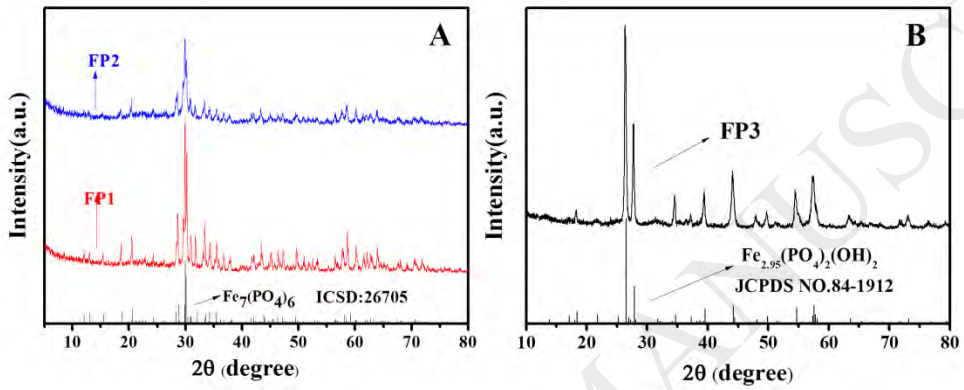

Figure 2. The XRD patterns of synthesized iron phosphates in different initial reaction concentration conditions: FP1 and FP2 (A), FP3 (B).

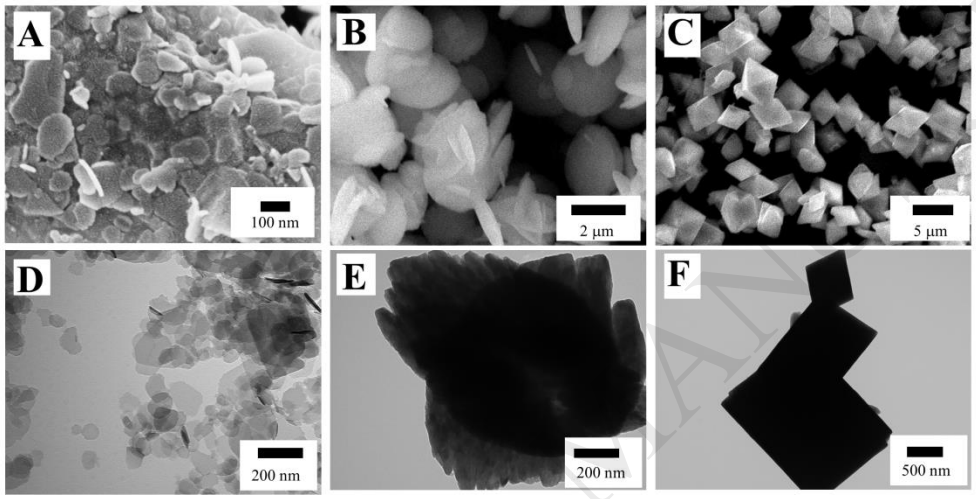

Figure 3. The SEM and TEM images of synthesized iron phosphates: FP1 (A) and (D), FP2 (B) and (E), FP3 (C) and (F).

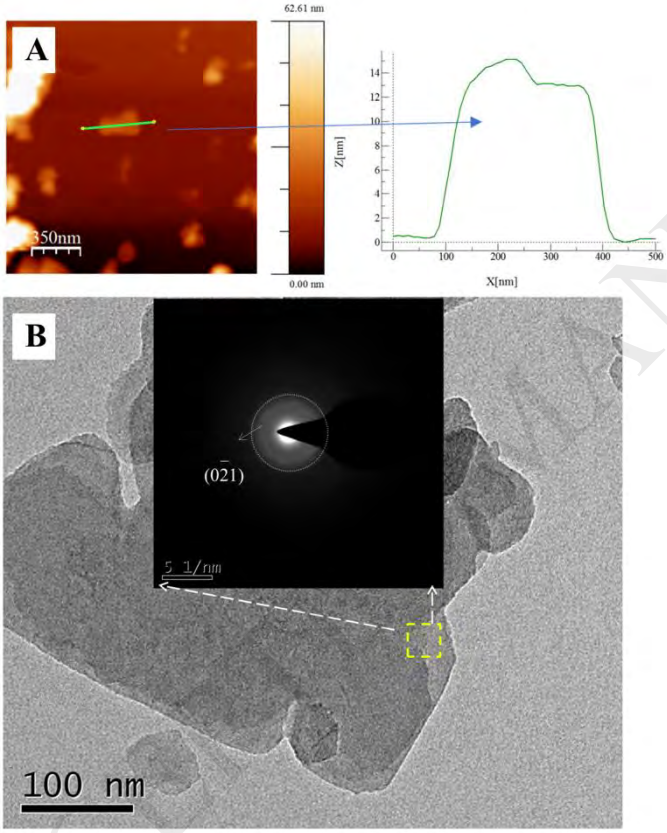

Figure 4. The AFM (A) and HRTEM (B) images of FP1.

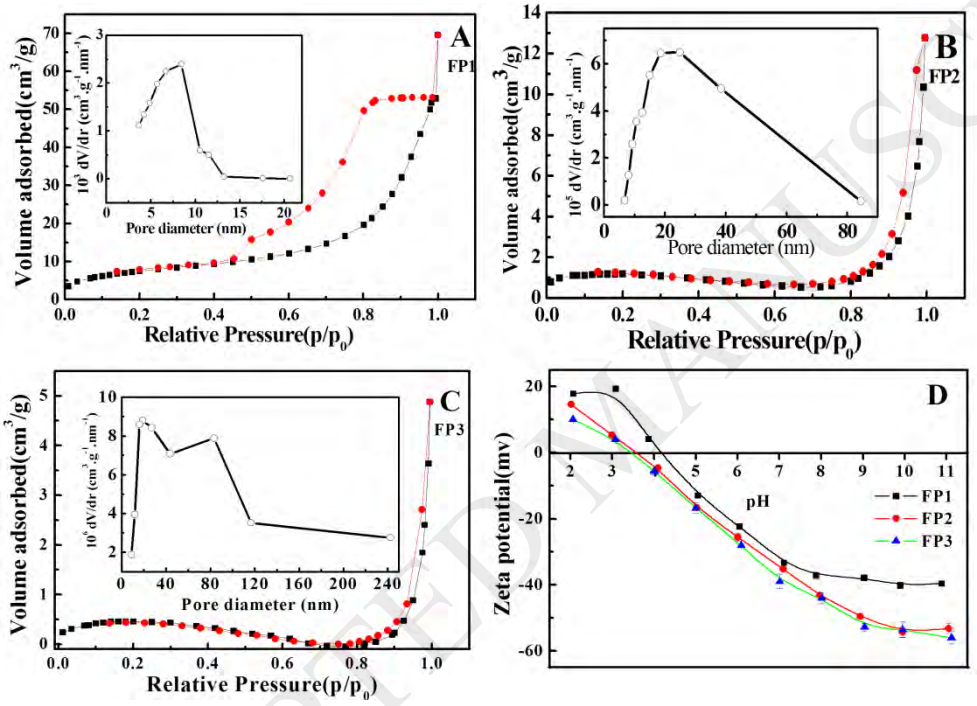

Figure 5. Nitrogen adsorption–desorption isotherms and corresponding BJH pore size distributions (insets) of synthesized iron phosphates FP1 (A), FP2 (B), FP3 (C). The zeta potentials of FP1, FP2 and FP3 (D) at various pH values.

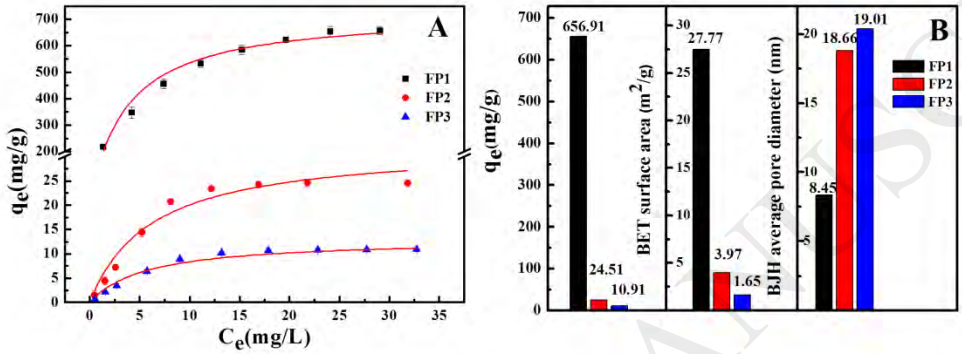

Figure 6. Adsorption isotherms of U(VI) by FP1, FP2 and FP3 (A), pH = 5.0 ± 0.1, m/V = 0.0167 g·L^{-1} (FP1), m/V = 0.667 g·L^{-1} (FP2 and FP 3), T = 308 K, equilibrium time = 24 h. Balanced adsorption capacity of removing U(VI)，intuitive comparison of surface areas and BJH average pore diameter of synthesized samples (B).

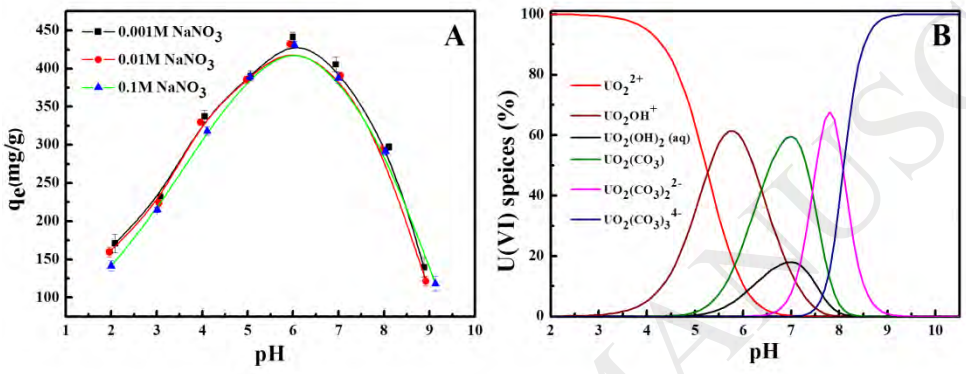

Figure 7. Effect of solution pH on the adsorption property of FP1 (A) 0.001, 0.01 and 0.1 mol·L^{-1} $NaNO_3$ solutions, m/V = 0.0167 g·L^{-1}, equilibrium time = 24 h, T = 298 K，C_0 = 20.0 mg·L^{-1} (U(VI)). The relative distribution of U(VI) species as a function of pH (B) in aqueous solutions.

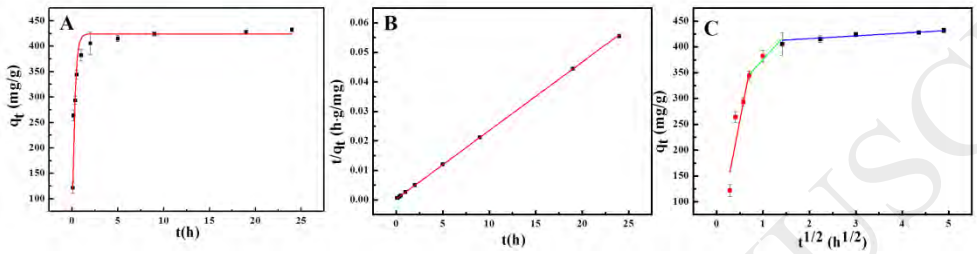

Figure 8. There different kinetic models fitted adsorption property of U(VI) by FP1 pseudo-first-order(A), pseudo-second-order(B), intra-particle diffusion model (C), T = 298 K, m/V = 0.0167 g·L^{-1}, C_0 =20.0 mg·L^{-1} (U(VI)), pH = 5.0 ± 0.1.

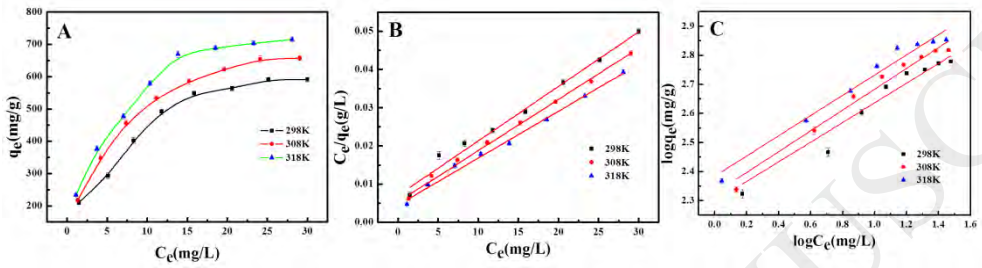

Figure 9. Adsorption isotherms of FP1 for U(VI) at different temperatures (A). Langmuir model (B) and Freundlich model (C) fitted the adsorption isotherms of U(VI). pH = 5.0 ± 0.1, m/V = 0.0167 g·L^{-1}, T = 298, 308, and 318 K, equilibrium time = 24 h.

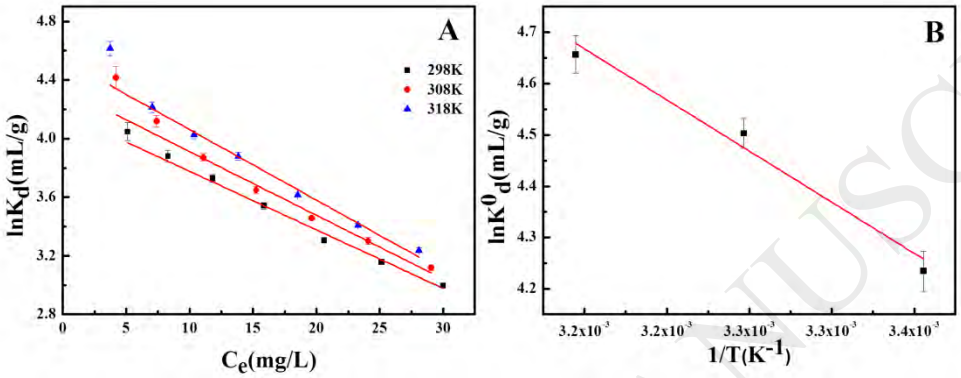

Figure 10. Relationship curve between $\ln K_d$ and C_e (A), Relationship curve $\ln K_d^0$ and 1/T (B), pH = 5.0 ± 0.1, m/V = 0.0167 g·L^{-1}, equilibrium time = 24 h.

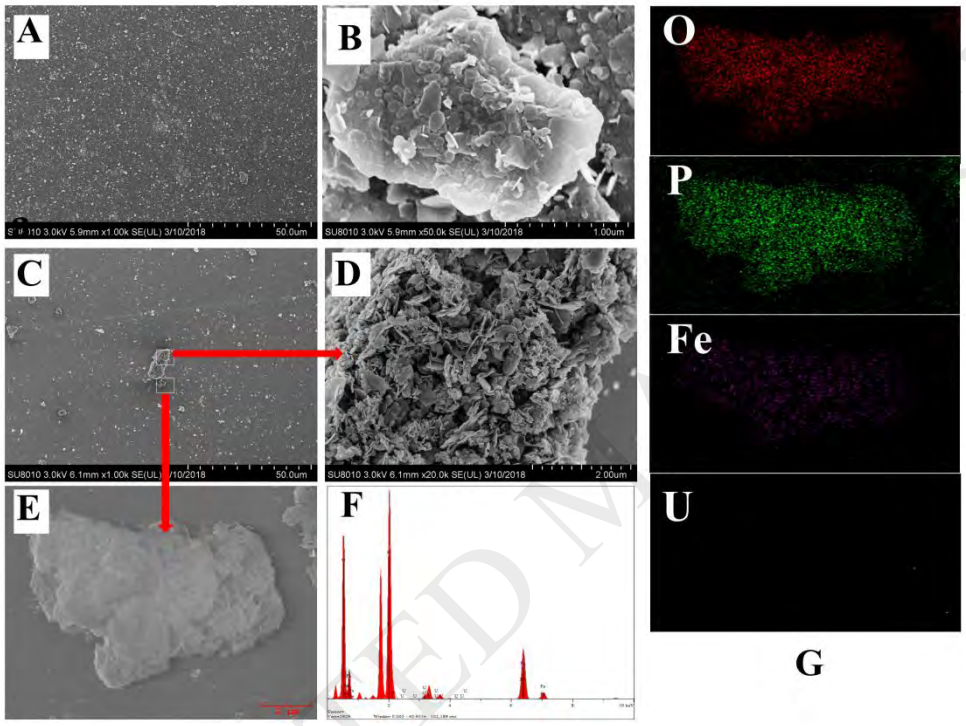

Figure 11. The FESEM images of FP1: before (A, B) and after (C, D and E) adsorption. The characterization of after adsorption samples, EDS (F) and Elementary mapping (G).

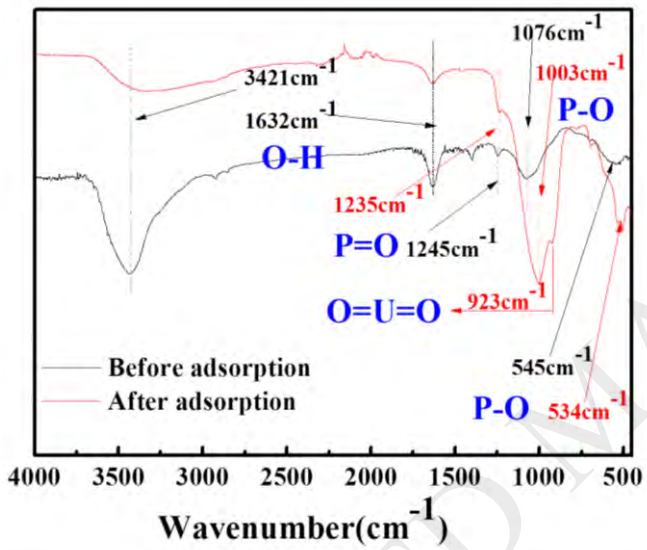

Figure 12. FT-IR of synthesized FP1: before and after adsorption.

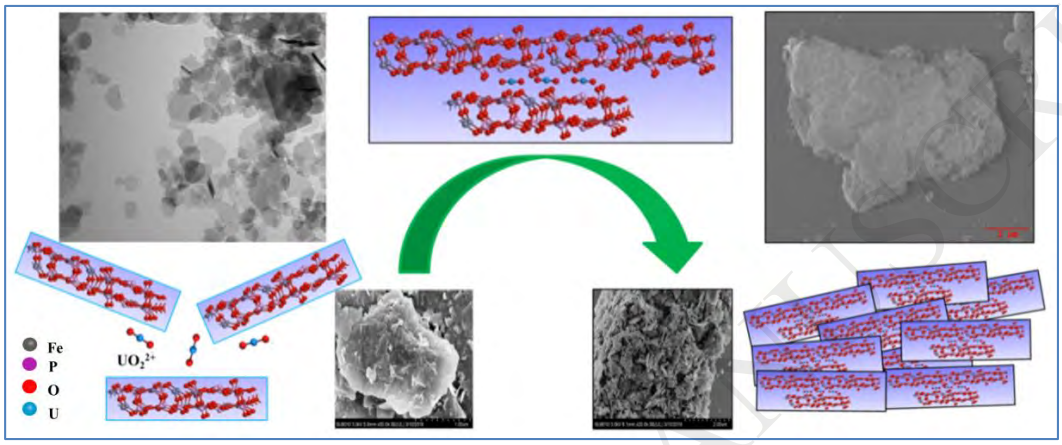

Figure 13. The possible adsorption progress of U(VI) by FP1.

Table 1. Kinetic parameters for the adsorption of U(VI) onto FP1.

Model		**Parameters**		**R^2**
Pseudo-first-order model	k_1	(h^{-1})	3.896	0.946
	q_e	($mg \cdot g^{-1}$)	424.162	
Pseudo-second-order model	k_2	($g \cdot mg \cdot h^{-1}$)	0.0173	0.999
	q_e	($mg \cdot g^{-1}$)	431.034	
Weber–Morris model	K_{int1}	($mg \cdot g^{-1} \cdot h^{-0.5}$)	467.318	0.810
	C_1	($mg \cdot g^{-1}$)	23.173	
	K_{int2}	($mg \cdot g^{-1} \cdot h^{-0.5}$)	98.446	0.880
	C_2	($mg \cdot g^{-1}$)	276.827	
	K_{int3}	($mg \cdot g^{-1} \cdot h^{-0.5}$)	5.338	0.855
	C_3	($mg \cdot g^{-1}$)	405.288	

Table 2. Langmuir and Freundlich isotherms parameters for U(VI) on FP1.

T	Langmuir model			Freundlich model		
	q_{max} (mg·g^{-1})	b (L·mol^{-1})	R^2_1	K_F (mol^{1-n}·L^n·g^{-1})	n	R^2_2
298 K	704.23	0.203	0.993	199.07	0.337	0.924
308 K	746.27	0.251	0.990	211.35	0.358	0.964
318 K	813.01	0.270	0.996	242.10	0.348	0.957

Table 3. Comparison of U(VI) adsorption capacities of FP1 with some sorbents.

Materials	**Experiment conditions**	**q_{max} ($mg \cdot g^{-1}$)**	**References**
ZrP_2O_7	pH= 2.8 ± 0.1, T=298 K	2.37	[38]
$Al_4(P_2O_7)_3$	pH= 5.5 ± 0.1, T=293 K	12.83	[22]
$Fe_4(P_2O_7)_3$	pH= 5.5 ± 0.1, T=293 K	14.92	[36]
Chitosan-tripolyphosphate	pH= 5.0 ± 0.1, T=298 K	236.9	[33]
PS-nG PAMAM-PPA	pH= 5.0 ± 0.1, T=298 K	106.58	[34]
Phosphoryl functionalized SiO_2	pH= 5.0 ± 0.1, T=288 K	197.8	[35]
MgFeAl-LDHs	pH= 5.0 ± 0.1, T=298 K	168	[82]
MoS_2-g-PDMA	pH= 4.0 ± 0.1, T=298 K	448.4	[51]
Ozonated GO	pH= 5.5 ± 0.1, T=303 K	291.8	[20]
Phosphate-functionalized GO	pH= 4.0 ± 0.1, T=303 K	251.7	[40]
$MnFe_2O_4$	pH= 5.0 ± 0.1, T=298 K	119.9	[84]
Perovskite	pH= 5.5 ± 0.1, T=303 K	119.3	[70]
polypyrrole	pH= 5.0 ± 0.1, T=298 K	87.72	[85]
pyrrhotite	pH= 4.0 ± 0.1, T=333 K	21.34	[86]
FP1	pH= 5.0 ± 0.1, T=298 K	704.23	this work

Table 4. Values of thermodynamic parameters for U(VI) adsorption onto FP1.

	ΔG^0 (KJ·mol^{-1})	ΔH^0 (KJ·mol^{-1})	ΔS^0 (J·mol^{-1}·K^{-1})
298 K	−10.49		
308 K	−11.16	16.57	91.01
318 K	−11.54		